REARRANGEMENT OF SECONDARY VORTICES OVER SPANWISE HETEROGENEOUS ROUGHNESS

A. Stroh,* *P. Forooghi and B. Frohnapfel*

Institute of Fluid Mechanics, Karlsruhe Institute of Technology, Karlsruhe, Germany

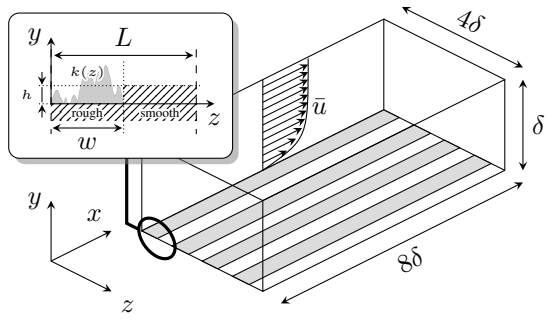

Figure 1: Schematic of the numerical domain with roughness strips at the walls.

Abstract

A spanwise heterogeneity of roughness is known to lead to the formation of large-scale secondary motions. In the present work the secondary motions are investigated based on the data sets extracted from direct numerical simulations (DNS) of fully developed turbulent open channel flow where spanwise-alternating streamwise stripes of rough and smooth surfaces with variation of the smooth surface elevation are introduced. In order to study the character of the secondary flow structures, the resultant flow fields are further analysed by means of instantaneous flow topology and by decomposition of the bulk mean velocity into its contribution parts. It is found that the wall-normal position of the smooth stripes significantly alters the secondary motion topology and strength of the motions. This alteration is also reflected in the fact that different volume flow rates are realized for different elevation heights of the smooth surface although the effective friction Reynolds numbers is kept constant.

1 Introduction

Prandtl's secondary flows of the second kind are known to be generated for rough-wall turbulent boundary layer flows with spanwise roughness heterogeneity. This fact is known since the pioneering work of (Hinze, 1973) and a good summary of recent work in this field is found in (Hwang & Lee, 2018). These secondary motions extend to the outer flow layer and significantly alter the mean-velocity profile. Similar observations were made in direct numerical simulations of turbulent channel flows with superhydrophobic surfaces (SHS) where streamwise stripes of a slip surface are introduced (Türk *et al.*, 2014). In case of SHS the presence of secondary motions results in a reduction of the flow rate when a turbulent channel flow driven by a constant pressure gradient (CPG) is considered. In the present work we aim at investigating the influence of secondary motions on the flow rate for flows over rough surfaces.

For rough-wall turbulent boundary layers opposite rotational directions are found for ridge- and strip-type roughness (Hwang & Lee, 2018) and in number of other investigations, see e.g. (Willingham *et al.*, 2014; Vanderwel & Ganapathisubramani, 2015), while a complete rearrangement of the secondary flow topology and reversal of the secondary motion direction are reported for SHS when the spanwise extend of the structure is increased (Stroh *et al.*, 2016).

The present contribution considers a detailed analysis of the secondary motions above a surface on which stripes of roughness are inserted as indicated in Figure 1. The space between roughness stripes is filled by a smooth surface with variation in elevation h relative to the channel wall. In Figure 2 such transitioning from a ridge type to a strip-type roughness is shown.

Topological evolution of the secondary flow and its properties are examined for variation of the smooth surface elevation, h, and compared to available literature results.

2 Procedure

A series of DNS has been carried out in a fully developed turbulent open channel flow in which the friction Reynolds number $\mathrm{Re}_\tau = u_\tau \delta(1-h_{\mathrm{eff}})/\nu = 500$ is kept constant. Here, $\delta(1-h_{\mathrm{eff}})$ represents the net channel height since h_{eff} is the average elevation of the surface nondimensionalized with channel half-height δ. As common in rough wall literature (Chan-Braun *et al.*, 2011) the friction velocity is evaluated at this position: $u_\tau(y = \delta h_{\mathrm{eff}})$. The code implementation is based on the incompressible pseude-spectral solver developed by Chevalier *et al.* (2007). The schematic of the numerical domain is depicted in Figure 1. Periodic boundary conditions are applied in streamwise and spanwise directions, while the wall-normal extension of the domain is bounded by no-slip boundary conditions at the lower domain wall ($y = 0$) and symmetry boundary condition ($v = 0$, $\partial u/\partial y = \partial w/\partial y = 0$) at the upper boundary ($y = \delta$). The domain size is

*Corresponding authors e-mail: alexander.stroh@kit.edu

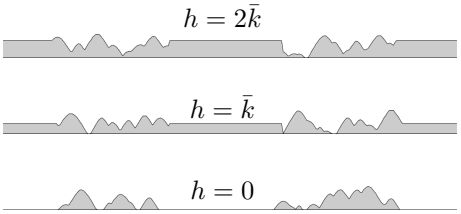

Figure 2: Roughness profiles $k(z)$ at a single location x for different elevation of the smooth stipes h.

$(L_x \times L_y \times L_z) = (8\delta \times \delta \times 4\delta)$ and the resolution is $(\Delta x^+ \times \Delta y^+_{min} \times \Delta z^+) = (5.2 \times 0.1 \times 5.2)$. The wave-length, L, represents the size of the alternating structure with a constant roughness fraction $\Phi = w/L = 0.5$, where w is rough stripe spanwise extent. Based on literature results the wave-length $L/\delta = 1$ is considered, for which the formation of a strong $(2 - 3\%U_b)$ large-scale secondary motion with pronounced generation of low- and high momentum pathways (LMP & HMP) is expected.

The rough and elevated smooth surfaces are modeled by introduction of an external volume force field to the Navier-Stokes equations based on the method proposed by (Goldstein *et al.*, 1993). The method is a variation of the direct forcing immersed boundary method (IBM), which imposes zero velocity in the solid region of the numerical domain utilizing a volume force given by:

$$F_i(x, y, z, t) = \alpha u_i(x, y, z, t) \quad \text{for} \quad y < k(x, z), \tag{1}$$

where $k(x, z)$ is the roughness elements height distribution and α is a negative constant that determines the relative strength of the applied force. For the roughness stripes we consider a homogeneous roughness distribution with mean surface elevation $\bar{k}/\delta = 0.041$, $k_{\text{max}}/\delta = 0.1$, $k_{\text{rms}}/\delta = 0.025$, skewness $Sk = 0.134$ and kurtosis $K = 2.21$ based on the rough areas only. The rough surface is generated using the technique proposed by Forooghi *et al.* (2017). Figure 2 shows three considered elevations of the smooth surface: $h = 0, \bar{k}$ and $2\bar{k}$. These three values might represent different roughness types (Bons *et al.*, 2001): roughness generated by deposition ($h = 0$, positively skewed for the entire wall area), roughness generated by simultaneous deposition and erosion ($h = \bar{k}$, near zero skewness) and roughness generated by pitting or erosion ($h = 2\bar{k}$, negatively skewed, "carved" roughness).

3 Results

Secondary Motion

Figure 3 presents the distribution of the mean velocity and the topology of the secondary vortices. The case with $h = 0$ presents a typical secondary motion for a ridge-type roughness. A significant modification of the secondary flow topology is evident when h changes: while an upward motion corresponding to LMP is observed over the rough stripe for $h = 0$, a downward motion or HMP is present over the rough stripes for $h > 0$. It has to be emphasized that the occurring secondary motion shows different strength - the maximum present velocity is $\sqrt{\bar{v}^2 + \bar{w}^2}/U_\infty = 1.8\%, 1.2\%$ and 2% for $h = 0, \bar{k}$ and $2\bar{k}$, respectively. The secondary motion is accompanied by a significant bulging of the streamwise mean velocity distribution, which is visible through the red isolines in Figure 3 and is especially evident in the outer region for $h = 0$ and $2\bar{k}$. At the same time the spanwise variation of $\bar{u}/U_\infty$ in the near-wall region is rather weak for $h = \bar{k}$ and $2\bar{k}$.

Instantaneous Flow Structure

In order to shed light on the nature of the secondary flow generation mechanisms in present turbulent simulations we consider a streamwise vortex detection in y-z-plane of instantaneous velocity fields. The algorithm is based on identification of swirling strength peaks followed by region growing routine for the estimation of the vortex extent (Vanderwel & Tavoularis, 2011). 1200 2d-velocity planes from 300 temporally uncorrelated 3d-velocity snapshots are utilized for the detection of the instantaneous streamwise vortices for each rough-wall simulation case.

Figure 4 demonstrates the spanwise PDF of the detected vortex centers. It has to be emphasized that the statistics contain only energetically significant vortices with swirling strength $\bar{\lambda}_{ci}$ larger than $2\%(\bar{\lambda}_{ci}\delta/U_\infty)_{\text{max}}$. Comparison of the considered cases reveals a similar total distribution of the detected vortices (grey histogram). However, if we plot the PDF of the vortices with positive (red) and negative (blue) rotational direction a spatial separation can be observed. The separation of the positively and negatively rotating instantaneous vortices is especially evident for $h = 2\bar{k}$ with positively rotating vortices concentrated within $z/\delta < 0.5$ and negatively rotating vortices withing $z/\delta > 0.5$. A separation of vortices is also visible for $h = 0$ while there is no clear trend for $h = \bar{k}$. The observed separation for $h = 0$ and $h = 2\bar{k}$ is in agreement with the structure of the secondary motion in figure 3 indicating that the observed large-scale secondary motion can be considered as a result of separation and clustering of smaller instantaneous vortices with the same rotational direction.

A more detailed view of the instantaneous vortex occurance is provided in Figure 5. It shows the difference between the PDF of positively and negatively rotating vortices for the same detection of instantaneous vortices in y-z-plane. It is evident that the location of vortex clusters with the same rotational direction coincides with the observed secondary flow depicted in Figure 3 also for case $h = \bar{k}$.

Impact on Total Shear and Bulk Mean Velocity

Utilizing a triple decomposition of the velocity

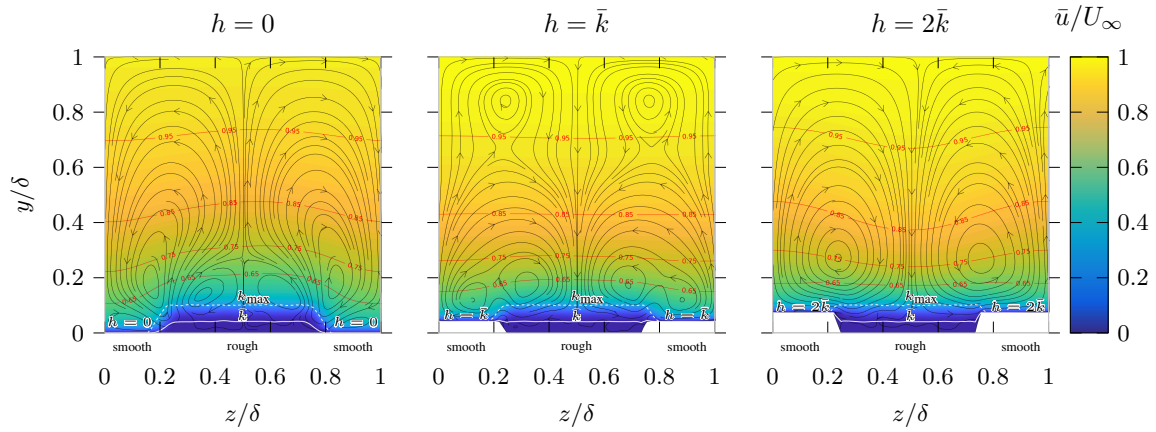

Figure 3: Mean velocity profile and secondary motions at different elevation of the smooth stripes h. Black arrows indicate time-averaged streamlines in y-z-plane, red solid lines mark the isolines for the streamwise mean velocity distribution.

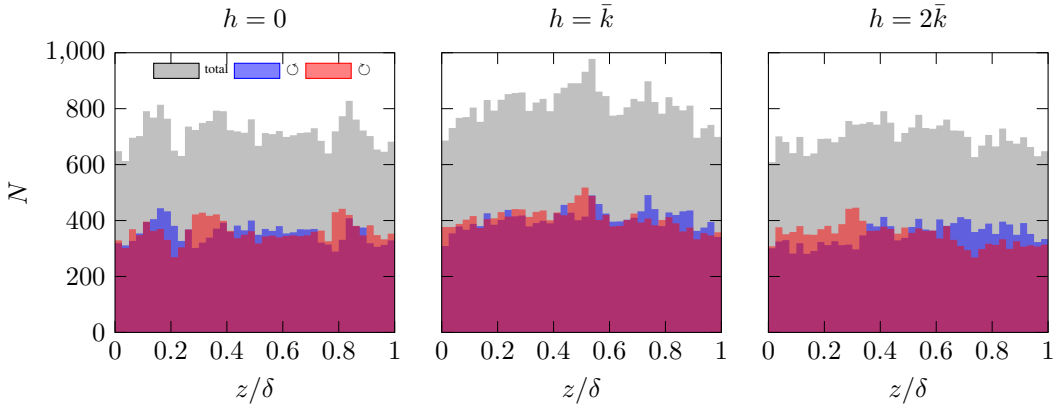

Figure 4: PDF of detected vortex centers.

field into mean part with dispersive ($\tilde{\cdot}$) and random ($\cdot''$) fluctuations as proposed by Reynolds & Hussain (1972):

$$u_i(x,y,z,t) = \langle \bar{u}_i \rangle (y) + \tilde{u}_i(y,z) + u_i''(x,y,z,t), \tag{2}$$

with time and streamwise averaging denoted by $\bar{\cdot}$ and spanwise averaging represented by $\langle \cdot \rangle$, the streamwise momentum balance can be written as

$$\underbrace{\frac{1-y}{1-h_{\text{eff}}}}_{\tau/\tau_{\text{eff}}} = \underbrace{\frac{1}{\text{Re}_\tau}\frac{\text{d}\langle\bar{u}\rangle^+}{\text{d}y^+}}_{\text{I}} \underbrace{-\langle\overline{u''v''}\rangle^+}_{\text{II}} \underbrace{-\langle\tilde{u}\tilde{v}\rangle^+}_{\text{III}} + \underbrace{\langle\bar{F}_x\rangle^+}_{\text{IV}}, \tag{3}$$

where h_{eff} is the reference plane position and $\tau_{\text{eff}} = \tau(h_{\text{eff}})$. The reference plane position h_{eff} is determined as the mean height of the entire roughness distribution, $k(x,z)$, including the elevated smooth wall regions. $\bar{F}_x$ represents the streamwise components of the IBM forcing. Figure 6 shows the corresponding decomposition of the total stress τ into its contributions. As expected, we observe a distinct peak for the forcing term (IV) in the IBM region. The viscous stress (I) clearly reflects the presence of the elevated surface. In all three cases the random stresses (II) form the major contribution to τ. The additional contribution from the dispersive fluctuations is evident for all three cases. However, the contribution is relatively weak and does not exceed 10% of the total stress locally. For $h = 0$ and $\bar{k}$ the contribution is present in the near-wall region ($y < 0.3$) only, while for the case with $h = 2\bar{k}$ the dispersive part protrudes up to $y = 0.6$. Interestingly, the distribution of the dispersive part remains positive for $h = 0$, negative for $h = \bar{k}$ and changes sign for $h = 2\bar{k}$. Similar behaviour of the dispersive component is shown by Türk *et al.* (2014) in a turbulent flow over SHS where a switch in the rotational direction of the secondary flow is observed.

Figure 7 shows the product of dispersive fluctuations $\tilde{u}\tilde{v}$ and random stress $\overline{u''v''}$. Spanwise integration of these maps provides the dispersive contribution and (random) turbulent contribution to the total stress in Figure 6. It is evident that the shift of the smooth wall position significantly changes the dispersive fluctuations - while for $h = 0$ and $\bar{k}$ the local fluctuation peaks are concentrated around the rough surface, for the highest smooth stripe position $h = 2\bar{k}$ positive peaks are evident in the outer flow. This translates into the non-zero dispersive contribution up to $y = 0.6$ in

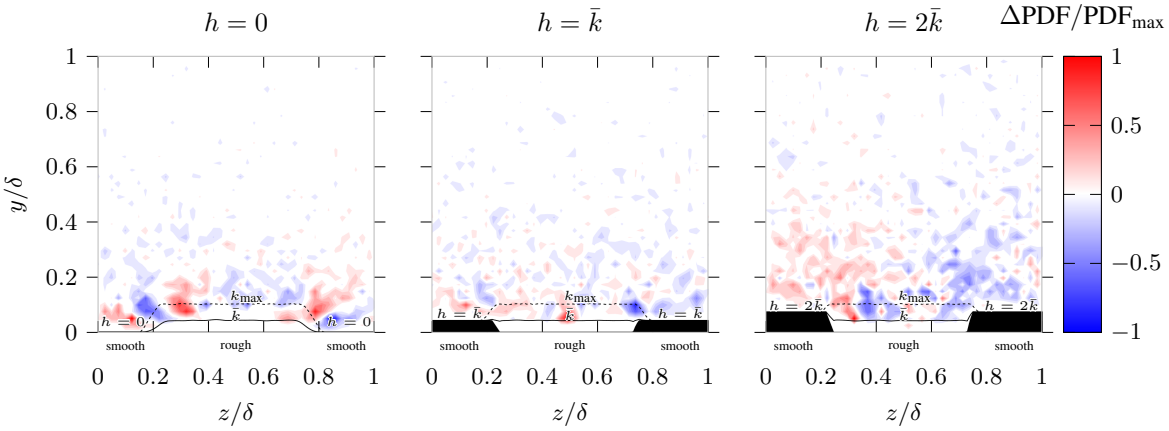

Figure 5: Difference of PDF distribution between detected centers of clock- and counterclockwise rotating vortices.

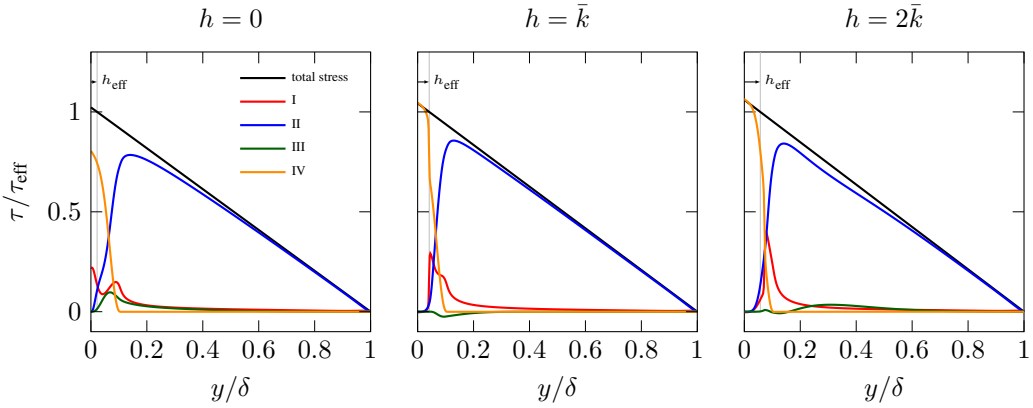

Figure 6: Total shear stress decomposition.

Figure 6.

In terms of the generated flow rate for the three considered cases the corresponding bulk Reynolds numbers are reported in table 1 in comparison to a smooth channel at the same Re_τ. As expected, in all rough wall cases Re_b is reduced compared to the smooth reference. The contributions to U_b^+ can be analyzed in a similar manner as the contributions to τ. Therefore, Eq. 3 is integrated twice. The resulting decomposition of the bulk mean velocity is similar to the one introduced by Marusic *et al.* (2007) or Benschop & Breugem (2017), and is given by:

$$\begin{aligned} U_b^+ &= \frac{1}{\delta(1-h_{\text{eff}})}\int_0^\delta \langle\bar{u}\rangle^+(y)\mathrm{d}y \\ &= U_b^L + U_b^R + U_b^D + U_b^F. \end{aligned} \tag{4}$$

U_b^L represents the laminar contribution

$$U_b^L = \frac{1}{(1-h_{\text{eff}})^3}\frac{\mathrm{Re}_\tau}{3}. \tag{5}$$

U_b^R and U_b^D are contributions related to turbulent stress $\langle\overline{u''v''}\rangle$ and dispersive fluctuations $\langle\tilde{u}\tilde{v}\rangle$:

$$U_b^R = \frac{1}{(1-h_{\text{eff}})^2}\int_0^\delta (1-y)\left\langle\overline{u''v''}\right\rangle \mathrm{d}y, \tag{6}$$

$$U_b^D = \frac{1}{(1-h_{\text{eff}})^2}\int_0^\delta (1-y)\left\langle\tilde{u}\tilde{v}\right\rangle \mathrm{d}y. \tag{7}$$

The last term, U_b^F, represents the contribution of the streamwise IBM forcing which can be understood as shear and pressure force exerted by the rough surface on the flow:

$$U_b^F = \frac{1}{(1-h_{\text{eff}})^2}\int_0^\delta (1-y)\left\langle\bar{F}_x\right\rangle \mathrm{d}y. \tag{8}$$

We recall that for a smooth-wall channel flow only the laminar contribution, U_b^L, and the contribution from the turbulent random fluctuations, U_b^R, are present, so $U_b^+ = U_b^L + U_b^R$ applies.

Table 1 lists the respective contribution to the bulk mean velocity in comparison to the reference smooth-wall channel flow. Due to the fact that the simulations are carried out with the same effective Re_τ but with different net channel heights the large positive laminar contribution, U_b^L, varies between the cases. This contribution represents the bulk mean velocity of a smooth wall laminar flow with the given channel height and driven by the pressure gradient that corresponds to the prescribed Re_τ.

As it is typically found in turbulent flows, this laminar contribution is opposed by a large negative contribution from the turbulent stress, U_b^R. Interestingly, the contribution is less pronounced for the rough cases in comparison to the smooth one. Rather small contributions arise from the dispersive contribution U_b^D. U_b^D is directly related to the presence of the secondary motion, which translates into a spatial variation of $\bar{u}$ and $\bar{v}$. It can be seen that case $h = 0$, where the largest U_b^D is found, exhibits the smallest value for U_b^R. This supports the previously mentioned observation that the secondary motions appear to consist of reorganized vortical structures. Once those structures contribute towards U_b^D, the total value of U_b^R is reduced. For $h = 0$ and $2\bar{k}$ the contribution of U_b^D is negative while it is positive in case $h = \bar{k}$. This difference in sign can be understood by carefully looking at the nature of the secondary motion in figure 7. In cases $h = 0$ and $2\bar{k}$ we mostly find upward motions in regions in which the mean streamwise velocity also bulges upwards. This indicates that relatively slow streamwise motion is transported upwards and thus suggests a negative correlation between $\tilde{u}$ and $\tilde{v}$. In the near-wall region of $h = \bar{k}$ one can identify regions in which upward motion and downward bulges in the mean streamwise velocity profiles co-exist (see left and right corner of the figure around $y/\delta = 0.1$). Those regions correspond to a positive correlation between $\tilde{u}$ and $\tilde{v}$ and thus also a positive value for U_b^D. Finally, the negative contributions of U_b^F directly reflect the fact that an increased area of the channel is exposed to IBM forcing which by definition opposes the flow rate.

4 Conclusions & Outlook

A DNS of spanwise-alternating rough-smooth surface with variation of smooth stripe elevation is conducted. For the current work the elevation of smooth stripe is fixed to $h = 0, \bar{k}$ and $2\bar{k}$. It is found that the topology of the secondary motion significantly differs depending on h. A switch of rotational direction can be observed between $h = 0$ and $h = 2\bar{k}$. The analysis of instantaneous vortex distributions reveals that the resulting secondary motions appears to originate from the redistribution of counter- and counterclockwise rotating instantaneous vortices. The decomposition of the resulting bulk velocity into its contributions suggests that secondary motions can positively influence the mean streamwise velocity. It remains to be investigated whether such a trend could be strengthened. However, as a first step is required to understand the generation mechanism of the secondary flows more thoroughly. We therefore plan to extend present work with analysis of the mean momentum budget as well as streamwise vorticity transport equation.

Acknowledgments

This work was performed on the computational resources bwUniCluster and ForHLR Phase II, funded by the Ministry of Science, Research and the Arts Baden-Württemberg, and the German Research Foundation (Deutsche Forschungsgemeinschaft, DFG) within the framework program bwHPC. The authors greatly acknowledge additional support by DFG through SFB/Transregio 150 project B02.

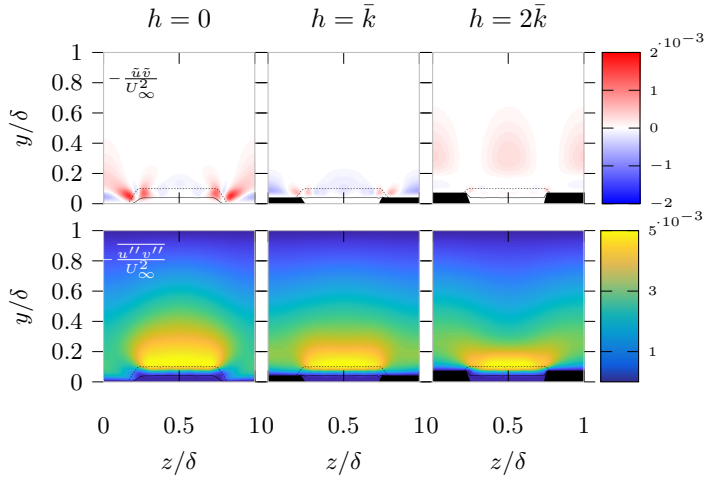

Figure 7: Product of dispersive fluctuations $\tilde{u}\tilde{v}$ and random fluctuations $\overline{u''v''}$.

Table 1: Composition of the bulk mean velocity for the reference case and three considered roughness distributions.

case	Re_τ	Re_b	U_b^+	U_b^L	U_b^R	U_b^D	U_b^F
smooth	500.1	18100	18.1	166.6	-148.5	0.0	0.0
$h = 0$	499.7	11512	11.5	178.1	-136.2	-6.6	-23.9
$h = \bar{k}$	499.6	11948	12.0	189.0	-146.9	1.2	-31.5
$h = 2\bar{k}$	499.7	12108	12.1	198.6	-144.3	-4.4	-37.8

References

Benschop, H. & Breugem, W. 2017 Drag reduction by herringbone riblet texture in direct numerical simulations of turbulent channel flow. *J. Turbul.* **18** (8), 717–759.

Bons, J., Taylor, R., McClain, S. & Rivir, R. 2001 The many faces of turbine surface roughness. In *ASME Turbo Expo 2001: Power for Land, Sea, and Air*, pp. V003T01A042–V003T01A042. American Society of Mechanical Engineers.

Chan-Braun, C., García-Villalba, M. & Uhlmann, M. 2011 Force and torque acting on particles in a transitionally rough open-channel flow. *J. Fluid Mech.* **684**, 441–474.

Chevalier, M., Schlatter, P., Lundbladh, A. & Henningson, D. S. 2007 Simson – a pseudo-spectral solver for incompressible boundary layer flows. *Tech. Rep.* TRITA-MEK 2007-07. KTH Stockholm, Stockholm, Sweden.

Forooghi, P., Stroh, A., Magagnato, F., Jakirlić, S. & Frohnapfel, B. 2017 Toward a universal roughness correlation. *J. Fluids Eng.* **139** (12), 121201.

Goldstein, D., Handler, R. & Sirovich, L. 1993 Modeling a no-slip flow boundary with an external force field. *J. Comput. Phys.* **105** (2), 354–366.

Hinze, J. O. 1973 Experimental investigation on secondary currents in the turbulent flow through a straight conduit. *Appl. Sci. Res.* **28** (1), 453–465.

Hwang, H. & Lee, J. 2018 Secondary flows in turbulent boundary layers over longitudinal surface roughness. *Phys. Fluids* **3** (1), 014608.

Marusic, I., Joseph, D.D. & Mahesh, K. 2007 Laminar and turbulent comparisons for channel flow and flow control. *J. Fluid Mech.* **570**, 467–477.

Reynolds, W. & Hussain, A. 1972 The mechanics of an organized wave in turbulent shear flow. Part 3. Theoretical models and comparisons with experiments. *J. Fluid Mech.* **54** (2), 263–288.

Stroh, A., Hasegawa, Y., Kriegseis, J. & Frohnapfel, B. 2016 Secondary vortices over surfaces with spanwise varying drag. *J. Turbul.* **17** (12), 1142–1158.

Türk, S., Daschiel, G., Stroh, A., Hasegawa, Y. & Frohnapfel, B. 2014 Turbulent flow over superhydrophobic surfaces with streamwise grooves. *J. Fluid Mech.* **747**, 186–217.

Vanderwel, C. & Ganapathisubramani, B. 2015 Effects of spanwise spacing on large-scale secondary flows in rough-wall turbulent boundary layers. *J. Fluid Mech.* **774**, 1–12.

Vanderwel, C. & Tavoularis, S. 2011 Coherent structures in uniformly sheared turbulent flow. *J. Fluid Mech.* **689**, 434–464.

Willingham, D., Anderson, W., Christensen, K. T. & Barros, J. M. 2014 Turbulent boundary layer flow over transverse aerodynamic roughness transitions: Induced mixing and flow characterization. *Phys. Fluids* **26** (2), 025111.